ACS Photonics

Article

pubs.acs.org/journal/apchd5

Ultrafast Optical Modulation of Second- and Third-Harmonic Generation from Cut-Disk-Based Metasurfaces

Giovanni Sartorello,[*,†] Nicolas Olivier,[†,⊥] Jingjing Zhang,[†,#] Weisheng Yue,[‡,◇] David J. Gosztola,[§] Gary P. Wiederrecht,[§] Grégory Wurtz,[†,∥] and Anatoly V. Zayats[†]

[†]Department of Physics, King's College London, Strand, London WC2R 2LS, United Kingdom

[‡]Advanced Nanofabrication, Imaging and Characterization Core Lab, King Abdullah University of Science and Technology, 4700 KAUST, Thuwal 23955-6900, Kingdom of Saudi Arabia

[§]Center for Nanoscale Materials, Argonne National Laboratory, 9700 South Cass Avenue, Argonne, Illinois 60439, United States

ABSTRACT: We design and fabricate a metasurface composed of gold cut-disk resonators that exhibits a strong coherent nonlinear response. We experimentally demonstrate all-optical modulation of both second- and third-harmonic signals on a subpicosecond time scale. Pump−probe experiments and numerical models show that the observed effects are due to the ultrafast response of the electronic excitations in the metal under external illumination. These effects pave the way for the development of novel active nonlinear metasurfaces with controllable and switchable coherent nonlinear response.

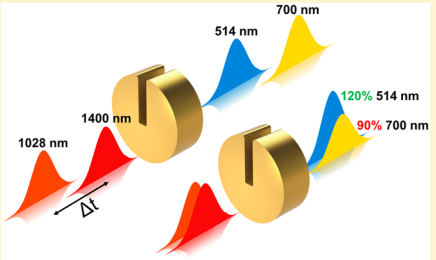

KEYWORDS: *nanophotonics, plasmonics, nonlinear optics, ultrafast optics, metasurfaces*

Metamaterials are artificial materials, assemblies of individual subwavelength units, which can exhibit properties not found in conventional materials. The archetypal example in optics is negative refraction,[1] but many other original effects have been proposed and demonstrated, including perfectly focusing superlenses,[2] subdiffraction imaging systems,[3] cloaking,[4] and enhanced nonlinearities.[5,6] Materials with controllable optical properties are highly sought after in nanophotonics, as they provide an avenue for designed, ultrafast control of light at the nanoscale,[7] leading to signal-processing systems with higher power efficiency, greater bandwidth, and faster response than semiconductor-based electronics allow.[8] Applications include all-optical circuits,[9] optical memory materials,[10] and digital metamaterials, which could lead to programmable all-optical systems.[11]

Typically weak nonlinear phenomena can be enhanced with plasmonic nanostructures utilizing field enhancement effects.[12] Nanoscale plasmonic structures exhibit "hotspots", which concentrate the energy carried by electromagnetic waves down to nanoscale volumes, providing a way to greatly enhance nonlinear generation efficiencies while also enabling extensive dispersion manipulation.[7]

Optical metasurfaces,[13] two-dimensional metamaterials of subwavelength thickness, are particularly well suited for light control in planar optical elements, with the potential to lead to compact, integrated nanodevices. Their thickness is a small fraction of that of any conventional optical component.[14] Although they are most commonly fabricated on thick substrates, flexible supports or membranes have also been used as substrates for metasurfaces.[15,16] Moreover, novel fabrication techniques have been developed[16−18] that are faster and cheaper than conventional electron-beam lithography, bringing large-scale production closer to practical requirements. Metasurfaces can control beam direction,[19−21] shape,[22] angular momentum,[23] polarization,[24,25] and both phase and polarization[26] and have been used for lensing[27] and holography.[28]

Optical switching has been demonstrated with metasurfaces in both electro-optical[29] and all-optical configurations.[6,30,31] In the latter case, a metasurface's optical response is affected by an optical control beam, whose effects can be measured, for example, as a change in the transmission or absorption of a probe beam. In these studies, subpicosecond switching times have been achieved in the extinction of metasurfaces.

Metasurfaces have also been studied in coherent nonlinear optics[32] for the efficient generation of second-[33] and third-harmonic signals.[34] In particular, since the thickness L of metasurfaces is subwavelength, the interaction length is typically much smaller than the coherence length, $L_{coh} = 2/\Delta k$,[35] and, therefore, phase matching is not a limiting factor for frequency mixing efficiency. Nonlinear planar metasurfaces may be suitable for applications in lasers and optical amplifiers, removing the need for expensive, high-grade macroscopic crystals, which require tedious alignment and millimeter-scale propagation distances. They would enable greater integration and increased portability. Frequency conversion can also be augmented with, for example, steering and switching, to create ultrafast, microscale nonlinear generators with integrated basic signal-processing capabilities, directional control, or both.

Special Issue: Nonlinear and Ultrafast Nanophotonics

Received: February 15, 2016
Published: June 6, 2016

DOI: 10.1021/acsphotonics.6b00108
ACS Photonics 2016, 3, 1517−1522

In this article, we combine efficient nonlinear generation with dynamic beam modulation on a single metasurface. We experimentally demonstrate ultrafast, all-optical modulation of both second-harmonic generation (SHG) and third-harmonic generation (THG) from nanoscale cut-disk resonator arrays. We explore the mechanisms governing the ultrafast coherent response of the metasurfaces by numerically modeling the time-dependent permittivity of the metal within the random phase approximation (RPA). Our results have important implications for the design of novel metasurfaces with coherent nonlinear response switchable on the picosecond time scale.

RESULTS

We studied metasurfaces consisting of arrays of gold nanoscale resonators. Gold (Au), widely used in nanophotonics, is centrosymmetric, prohibiting bulk SHG in the dipolar approximation. The symmetry of the Au crystal lattice is broken at the surface, so that surface effects dominate the second-order nonlinear response, making Au nanostructures possible SH sources.[36] A metallic split-ring resonator (SRR) is widely used as the unit cell for metasurfaces in the optical and near-IR spectral ranges, where it exhibits multiresonant behavior.[37] Moreover, SRR arrays show strong polarization-dependent second-[33] and third-harmonic[34] generation. The unit cell of the metasurfaces studied here (Figure 1a) contains a

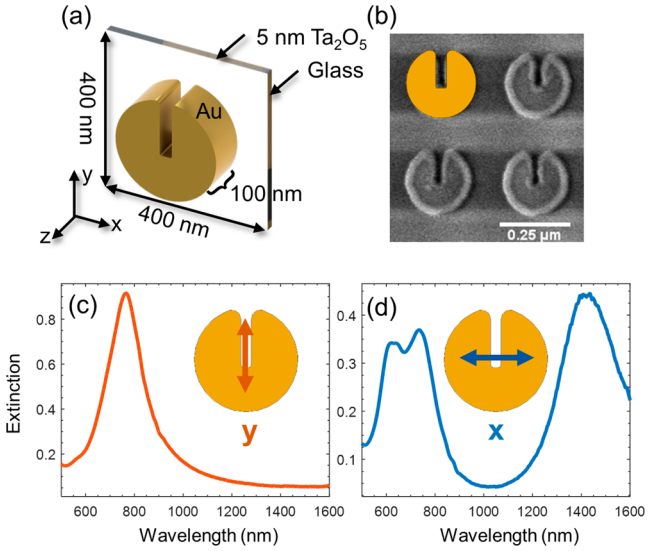

Figure 1. Cut-disk metasurface and linear optical properties. (a) Unit cell geometry. (b) Low-voltage SEM micrograph of a 2 × 2 subunit of the array. Au nanodisks are 250 nm in diameter and 100 nm high. They are cut partway with a slit 30 nm wide and 140 nm long and form 60 × 60 μm^2 arrays. (c, d) Experimental extinction spectra for light polarized (c) along and (d) across the slit. The orientation of the incident wave's electric field is indicated in the insets.

Au disk, 250 nm in diameter and 100 nm in height, with a 140 nm long and 30 nm wide slit cut partway through it. Figure 1b shows a typical SEM micrograph of a 2 × 2 subunit of the array. In this geometry, the symmetry of a disk-shaped nanoparticle is broken, enabling the linear multiresonant response of the unit cell, as well as its unique coherent nonlinear behavior.

Linear Optical Properties. To first approximation, a disk supports two nondegenerate dipolar electric resonances, with the dipolar moment either along or perpendicular to the axis of the disk. Given that the distance between neighboring particles is relatively large when compared to the particle's modal volume, these arrays can be described within the weak coupling regime as the coherent response of isolated resonators. For normally incident light along the *z*-axis, a uniform disk-shaped particle exhibits a single dipolar resonance,[38] which is degenerate with polarization. This dipolar response is drastically modified when a slit is introduced along the diametric axis of the disks. Two different polarization-sensitive optical responses arise, one with the electric field of the incident wave along the slit ("*y*" direction in Figure 1c) and the other with the electric field across it ("*x*" direction in Figure 1d).

In the former case, the extinction spectrum is similar to that of disk-shaped particles, with a single dipolar resonance around 765 nm. In the latter case, the resonance in the same spectral range is blue-shifted by about 90 nm and assumes a double-peak Fano shape. This shape is due to the interference between the dipolar and the quadrupolar modes supported by the disk-shaped particle. The quadrupolar resonance is dark in a symmetric disk-shaped particle, but the introduction of the slit creates an imbalance in the quadrupolar moment, leading to the appearance of a net dipole moment, making it accessible to incident light through dipolar coupling. The resulting superposition of the spectrally overlapping disk-shaped modes causes an apparent decrease in the extinction of the cut-disk nanoparticle response at frequencies where the two moments interfere destructively. For this geometry the dipole and quadrupole modes of the disk-shaped particle are mixed and form a Fano-type mode. The introduction of the slit also leads to the appearance of a new resonance in the near IR at around 1400 nm. This resonance, also present in square SRRs, is often associated with a magnetic dipole oscillating along the light propagation direction (*z*-axis) and created by the electrically driven charge oscillations of a solenoid-like current across the particle, resulting in a charge buildup of opposite sign on opposite sides of the slit.[39] This resonance provides the enhancement of the electromagnetic field for the generation of coherent nonlinear signals.

Transient Linear Optical Properties. Upon excitation with ultrashort optical pulses, the linear optical properties of the metasurface and, as a result, its coherent nonlinear response can be modulated via a transient nonequilibrium Au electron energy distribution, resulting in a change in the metal's permittivity.[6] The transient differential extinction (ΔOD) of the metasurfaces (Figure 2a; see Methods for experimental details) reveals a sequence of alternating bands of induced extinction (positive ΔOD) and induced transparency (negative ΔOD) occurring at different wavelengths and time scales. The simulated transient ΔOD spectra (Figure 2b,c; see Methods for the details of the simulations) clearly recover the main features of the experiment. The ground-state simulated extinction (Figure 2d, solid blue line) reproduces the features of the experimental *x*-polarized extinction (Figure 2f), with the presence of the Fano resonance at visible wavelengths and the magnetic dipole resonance in the near-IR range. Small deviations in the optical response of the simulated and measured structures in both the spectral position and linewidth of the resonances are due to variations in shape and size between particles that affect the position and lead to inhomogeneous broadening of the resonance.[40,41]

The excited state extinction (Figure 2d, dashed line) and differential extinction (Figure 2e), at a time at which maximum optical modulation is achieved, show a magnetic dipole resonance at around 1400 nm with a clear dispersive behavior,

DOI: 10.1021/acsphotonics.6b00108
ACS Photonics 2016, 3, 1517−1522

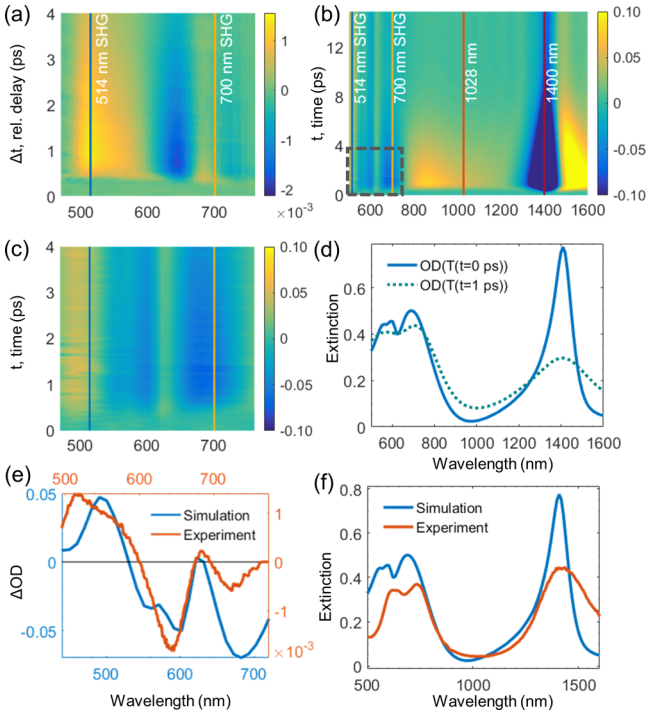

Figure 2. Transient linear optical response. (a) Experimental and (b, c) simulated transient differential extinction (ΔOD). The *x*-polarized control light wavelength is 465 nm. Solid lines mark the wavelengths used for nonlinear transient measurement in Figure 4. The range of the experimental measurements in (a) and corresponding simulations in (c) is shown in the extended simulated map in (b) with a gray dashed line. (d) Simulated extinction spectra in the ground (t = 0 ps) and excited (t = 1 ps) states. (e) Normalized ΔOD for the excited state obtained from the experiment (Δt = 0.8 ps) and simulation (t = 1 ps). Note that the experimental and simulated spectra are shifted by 55 nm to compare corresponding features, as the simulated particle has slightly shifted resonances. (f) Simulated and experimental ground-state extinctions.

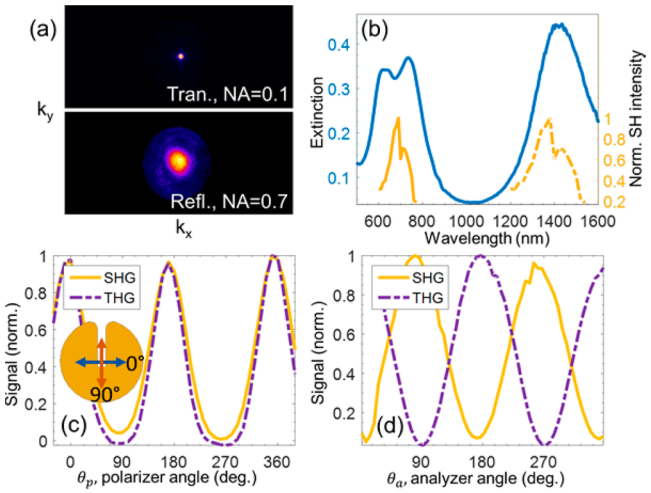

Figure 3. Nonlinear response. (a) CCD images of the emitted 700 nm SHG in transmission (top) and reflection (bottom) measured with different NA objectives. (b) Extinction (blue) and SHG (yellow) spectra for *x*-polarized fundamental light. The SHG spectra are plotted with respect to both fundamental (dashed line) and SH (solid line) wavelengths. (c) SHG and THG intensity dependences on the polarization of the incident fundamental light. (d) Polarization of the emitted SHG and THG for the fundamental light polarization across the slit (*x*-polarization, ϑ_p = 0°). (a), (c), and (d) were measured with a fundamental light of 1400 nm. The data in (b)−(d) are measured in transmission.

mainly governed by a combined red-shift and an increased damping of the resonance following optical excitation. The transient response of the Fano resonance is more complex: because of an increased damping for the underlying dipolar mode and radiative loss for the quadrupolar mode, the resonance becomes broader, leading to a loss of coherence between the two resonances and a shallower Fano dip. In the intermediate spectral range (800 to 1200 nm), an induced increased extinction is observed, mainly due to the broadening of both electric and magnetic resonances.

The extinction corresponding to the magnetic resonance experiences a substantial modulation, decreasing by about 60% at 1400 nm, while the extinction at the Fano resonance changes by a comparatively smaller value of up to 20% at 690 nm. This difference reveals the relatively stronger sensitivity of the field associated with the magnetic resonance to transient changes in the particle's permittivity. This observation is key to understanding the resulting transient coherent response outlined below.

Coherent Nonlinear Optical Properties. The cut-disk array behaves as an assembly of in-phase resonators, coherently interacting so as to produce a nonlinear far-field emission diagram with a circular angular spread dependent upon the numerical aperture (NA) of the illumination objective as shown in transmission and reflection measurements (Figure 3a). The SHG spectrum (Figure 3b) shows a double-resonant behavior,[42,43] indicating the importance of the resonances at both fundamental and SH wavelengths and recovering qualitatively the shape of the Fano resonance.

Both SHG and THG signals have maximum emission for an incident polarization across the slit (Figure 3c). In fact, the outgoing intensities of SHG and THG follow a $\sin^4(\vartheta_p)$ and $\sin^6(\vartheta_p)$ trend, respectively, where ϑ_p is the polarization angle of the fundamental light with respect to the *y*-axis, with at least a two-order of magnitude difference between minima and maxima. This is due to the $\sin^2(\vartheta_p)$ and $\sin^3(\vartheta_p)$ dependence of the fundamental light intensity in the respective nonlinear polarizations. We therefore used the fundamental light polarized across the slit (*x*-polarization) in all the following measurements.

The emitted SHG and THG signals have orthogonal linear polarizations, with THG polarized across the slit, the same as the polarization of the incident fundamental beam, and SHG polarized along the slit, i.e., rotated 90° with respect to the polarization of the fundamental light (Figure 3d). Thus, the dominant tensor component for the effective second- and third-order nonlinear susceptibilities are $\chi^{(2)}_{y;xx}$ and $\chi^{(3)}_{x;xxx}$, respectively, where the first index refers to the output polarization and the remaining indices describe the polarization of the input beams, i.e., the degenerate fundamental beam in this instance.

All-Optical Modulation of Nonlinear Processes. Ultrafast pump−probe experiments were performed to study the transient response of the coherently generated nonlinear signals. The experimental setup (Figure 4a, details in Methods) uses a two-color 200 fs pulsed excitation with a 1400 nm fundamental probe beam (ω_1) and a 1028 nm control light (ω_2). The relative time delay (Δt) between the pulses is scanned over a range of several picoseconds. The spectrum of the nonlinear response of the metasurface obtained for Δt = 0,

DOI: 10.1021/acsphotonics.6b00108
ACS Photonics 2016, 3, 1517−1522

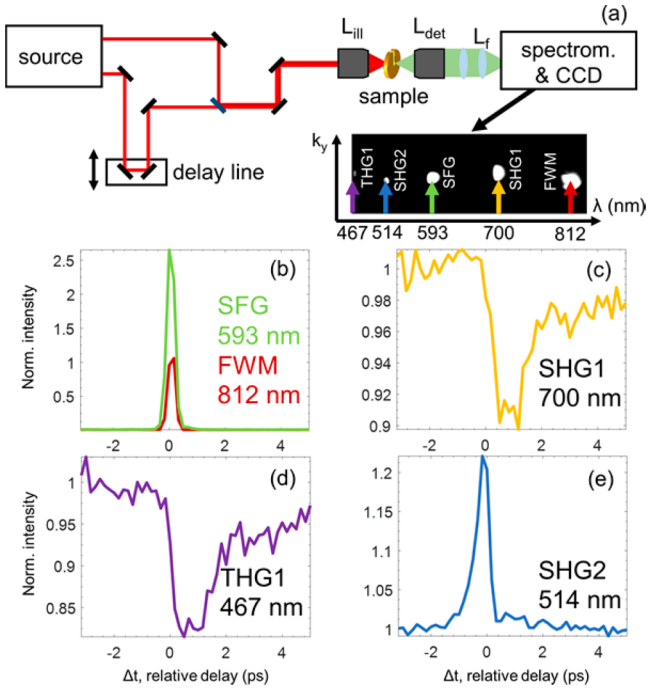

Figure 4. Ultrafast all-optical modulation of coherent nonlinear signals. (a) Schematic of the ultrafast pump–probe setup. The inset shows the spectrum of the nonlinear signals observed on the CCD for simultaneously overlapping (Δt = 0) fundamental (1400 nm) and control (1028 nm) pulses: $\lambda(2\omega_1)$ = 700 nm (SHG1), $\lambda(2\omega_2)$ = 514 nm (SHG2), $\lambda(\omega_1 + \omega_2)$ = 593 nm (SFG), $\lambda(3\omega_1)$ = 467 nm (THG1), and $\lambda(2\omega_2 - \omega_1)$ = 812 nm (FWM). (b–e) Transient behavior of (b) SFG and FWM, (c) SHG1, (d) THG1, and (e) SHG2. For (c)–(e) the SHG and THG data are normalized to the signal intensity at $|\Delta t| \rightarrow \pm\infty$. FWM and SFG signals in (b) are normalized relative to the 700 nm SHG signal.

when fundamental and control beams are superimposed both spatially and temporally, reveals a series of nonlinear processes (Figure 4a).

When the fundamental and control pulses are not overlapping in time ($\Delta t \rightarrow \pm\infty$), only nonlinear harmonics from the fundamental and control beams (ω_1, ω_2) are detected. These include the 700 nm SHG1 and 467 nm THG1 from the 1400 nm probe beam as well as the 514 nm SHG2 from the 1028 nm control beam. As the temporal overlap between the beams is achieved ($\Delta t \rightarrow 0$), two more coherent signals, corresponding to sum-frequency generation (SFG, $\omega_1 + \omega_2$) and four-wave mixing (FWM, $2\omega_2 - \omega_1$), are also observed (Figure 4b). These two signals, therefore, offer a convenient synchronization fingerprint. The dynamics of the single-beam coherent response reveal two differing behaviors. The SHG1 at 700 nm (Figure 4c) experiences a 10% decrease in intensity at $\Delta t \approx 0$, induced by the control beam. A similar behavior is observed for the 467 nm THG1 (Figure 4d), with both signals recovering their steady-state intensity over a time scale of several tens of picoseconds. The temporal response is consistent with an optically induced change in the metal's permittivity recovery through electron–phonon and phonon–phonon relaxation processes. In contrast, the transient SHG2 excited by the control beam itself at 514 nm (Figure 4e) is enhanced, with a 20% increase in intensity and the relaxation at a time scale of roughly 0.4 ps, much faster than the 700 nm SHG1.

Analysis and Discussion. The transient signals of Figure 4c–e are governed by the transient dependencies of both the nonlinear susceptibility of the respective coherent processes and the local amplitude of the fundamental field driving them. This is explicit from the expressions of the nonlinear polarizations $P^{(2)}(2\omega) = \varepsilon_0\chi^{(2)}(2\omega; \omega, \omega)E_l^2(\omega)$ for SHG and $P^{(3)}(3\omega) = \varepsilon_0\chi^{(3)}(3\omega; \omega, \omega, \omega)E_l^3(\omega)$ for THG, where $E_l(\omega) = \alpha(\omega)E_0(\omega)$ is the local driving field at the fundamental frequency, with $\alpha(\omega)$ being the cut-disk linear polarizability. While both $\partial\chi/\partial E_c$ and $\partial\alpha/\partial E_c$, where E_c is the control field, contribute to the transient response, it is clear from the hierarchy of nonlinear susceptibilities and numerical modeling that the local driving field modification under the influence of the control light is dominating the transient behavior of the nonlinear signals. As one can see from Figure 2d, the polarizability of the cut disk at a wavelength of 1400 nm is significantly decreased under the control illumination due to the damping and red-shift of the magnetic resonance, leading to a decrease in the SHG amplitude around $\Delta t \approx 0$ (Figure 4c). The relatively slow recovery of the signal reflects the resonant behavior of the particle at 1400 nm. A similar argument can be made to explain the transient THG signal of Figure 4d, although, *a priori*, there is a noticeable difference between the two processes since the SHG at 700 nm is doubly resonant at both the fundamental and SH frequencies, while the THG process is resonant only at the fundamental frequency. The fact that a similar transient response is evident for both signals strengthens the argument that the main mechanism controlling both the decrease and the recovery dynamics of the processes is the ultrafast transient behavior of the local field at the fundamental frequency.

This analysis is further supported by the transient response of the 514 nm SHG2 signal in Figure 4e, showing the SH signal from the control beam at 1028 nm modulated by the simultaneous presence of the probe beam at 1400 nm. This is evidence that, regardless of the intended assignment of control and probe, both beams affect the permittivity of the plasmonic resonators, and their associated nonlinear coherent signals probe those changes. In Figure 4e, both the fundamental and SHG light are nonresonant with the structure, showing a dynamics with an increase in the 514 nm signal followed by a rapid decay to the $\Delta t \rightarrow \pm\infty$ level. The mirror symmetry of the transient response of the 700 nm and 514 nm SHG signals with respect to t = 0 is due to the relative arrival time of the corresponding fundamental beams on the sample, with the 1028 nm beam reaching the sample before the 1400 nm beam. The sub-picosecond relaxation time of the 514 nm SHG2 signal is faster than the multi-picosecond relaxation time of the 700 nm SHG1 (Figure 4c,e). This is related to the faster relaxation of the nonlinear response observed in the linear transient spectra (Figure 2b) at the off-resonance wavelength of 1028 nm than at the resonant wavelength of 1400 nm.

CONCLUSIONS

We studied the ultrafast transient behavior of multiresonant plasmonic nanostructures acting as nonlinear coherent emitters. SHG and THG signals emitted by the cut-disk resonators for both resonant and nonresonant input and output frequencies have been shown to experience an ultrafast modulation of their intensity at the picosecond time scale under optical control. The transient incoherent response of the resonators provided a rationale for these observations in both the sign of the intensity modulation of the coherent nonlinear signals and the respective

DOI: 10.1021/acsphotonics.6b00108
ACS Photonics 2016, 3, 1517–1522

relaxation times. In particular, we found that the transient response is governed by the ultrafast response of the electronic density in the metal and its impact on the optical properties of the plasmonic resonators at the fundamental frequency. These results show frequency conversion and its optical nonlinear control combining coherent and Kerr-type nonlinearities of plasmonic nanostructures. As the metasurfaces show directional emission typical of phase-locked resonators, the observed effects can be used for beam steering and directionality control of generated harmonics to allow output harmonic separation with collinear single beam inputs. Further extension of this work may include controlled beam shaping to achieve switchable wavefront generation of nonlinear harmonics.

METHODS

Fabrication. Gold nanostructures were fabricated on a glass substrate via electron beam lithography (EBL) and plasma etching. Exposed negative resist ma-N 2400 was used as the etching mask. After the etching, the residual was cleared with acetone followed by oxygen plasma cleaning. To guarantee the structural stability of the nanostructures, a 5 nm Ta_2O_5 adhesion layer was deposited by sputtering on the substrate prior to metal lithography. Several arrays were fabricated, on the same sample, with slightly different exposure dose and geometry. For all measurements shown, the array period is 400 nm and the area is 60 × 60 μm^2. AFM measurements show a typical surface roughness of 10%. SEM measurements required low accelerating voltages (2 kV) because the substrate is poorly conductive.

Measurements. For linear transmission measurements, a halogen lamp was used together with polarization optics and a fiber-coupled spectrometer. Extinction is defined as OD = $-\log_{10}(T/T_0)$, where T is the transmittance of the array and T_0 is a reference transmittance measured through the substrate alone. Raw extinction spectra show uniform 10% noise, which was removed through LOESS interpolation. The setup for nonlinear transmission and pump−probe experiments (Figure 4a) is built around an ultrafast laser source consisting of an amplified ultrafast oscillator (Pharos, Light Conversion) delivering 200 fs pulses at a central wavelength of 1028 nm. This amplified output beam is split in two arms, with roughly half the original 15 W power pumping an OPA (Orpheus, Light Conversion), which generates a frequency-tunable beam. The remaining half of the 1028 nm beam is sent to the sample via a delay line (Thorlabs) that controls the relative arrival time Δt of the beams onto the sample. Suitable optical components placed in both beam paths allow for independent control of polarization, power, divergence, and size of the two beams before they are focused onto the sample. For the SH measurements, the fundamental peak irradiance at the sample surface was about 4 GW/cm^2, while it was about 2 GW/cm^2 for both beams during pump−probe experiments. The laser-induced damage threshold of the samples was observed at peak irradiances of about 10 GW/cm^2. The residues of the fundamental incident beams are filtered out after the sample using band-pass filters (Thorlabs). For SHG spectroscopy, the OPA output was tuned to the desired fundamental frequencies. The transient differential extinction measurements were performed using a 100 fs amplified Ti:sapphire laser (Spectra Physics) to generate a 467 nm pump through an OPA (Light Conversion) and a white light continuum (approximately 470−760 nm wavelength range) probe generated using a sapphire crystal. A spatial filter in Fourier space was used to filter out the pump beam and collect the transmitted probe only.

Simulations. The FDTD simulations of Figure 2b−f use Lumerical's FDTD Solutions package. The simulated structure's dimensions were taken to be the average sizes obtained through SEM and AFM measurements, resulting in a close match between the extinction peak positions between simulation and linear transmission measurement. However, structure-by-structure variability and fabrication imperfections cause slight shifts and broader peaks in the real case. This does not affect the general behavior induced in the all-optical modulation experiments. The extinction modulation simulations use uniform, temperature-dependent permittivity obtained with a method previously described in detail.[6] In such a model, electron−electron scattering occurring at very short time scales of tens of femtoseconds is neglected, while the experiments do not have the time resolution required to observe these effects.

AUTHOR INFORMATION

Corresponding Author

*E-mail: giovanni.sartorello@kcl.ac.uk.

Present Addresses

[⊥]Department of Physics and Astronomy, University of Sheffield, Hicks Building, Hounsfield Road, Sheffield, S3 7RH, United Kingdom.

[∥]Department of Physics, University of North Florida, 1 UNF Drive, Jacksonville, Florida 32224, United States.

[#]School of Electrical and Electronic Engineering, Nanyang Technological University, Nanyang Avenue, 639798, Singapore.

[◇]National Graphene Institute, University of Manchester, Oxford Road, Manchester M13 9PL, United Kingdom.

Author Contributions

All authors have given approval to the final version of the manuscript.

Notes

The authors declare no competing financial interest.

ACKNOWLEDGMENTS

This work was supported, in part, by EPSRC (UK) and the ERC iPLASMM project (321268). J.Z. was supported by the Royal Society Newton International Fellowship. A.Z. acknowledges support from the Royal Society and the Wolfson Foundation. G.W. acknowledges the support from the EC FP7 Project No. 304179 (Marie Curie Actions). Use of the Center for Nanoscale Materials, an Office of Science user facility, was supported by the U.S. Department of Energy, Office of Science, Office of Basic Energy Sciences, under Contract No. DE-AC02-06CH11357. All data supporting this research are provided in full in the Results section.

REFERENCES

(1) Pendry, J. B.; Smith, D. R. Reversing light with negative refraction. *Phys. Today* **2004**, *57*, 37−43.

(2) Pendry, J. B.; Ramakrishna, S. A. Focusing light using negative refraction. *J. Phys.: Condens. Matter* **2003**, *15*, 6345−6364.

(3) Fang, N.; Lee, H.; Sun, C.; Zhang, X. Sub-diffraction-limited optical imaging with a silver superlens. *Science* **2005**, *308*, 534−7.

(4) Cai, W.; Chettiar, U. K.; Kildishev, A. V.; Shalaev, V. M. Optical cloaking with metamaterials. *Nat. Photonics* **2007**, *1*, 224−227.

(5) Shadrivov, I. V.; Zharov, A. a.; Kivshar, Y. S. Second-harmonic generation in nonlinear left-handed metamaterials. *J. Opt. Soc. Am. B* **2006**, *23*, 529−534.

DOI: 10.1021/acsphotonics.6b00108
ACS Photonics 2016, 3, 1517−1522

(6) Wurtz, G. A.; Pollard, R.; Hendren, W.; Wiederrecht, G. P.; Gosztola, D. J.; Podolskiy, V. A.; Zayats, A. V. Designed ultrafast optical nonlinearity in a plasmonic nanorod metamaterial enhanced by nonlocality. *Nat. Nanotechnol.* **2011**, *6*, 107−11.
(7) Kauranen, M.; Zayats, A. V. Nonlinear plasmonics. *Nat. Photonics* **2012**, *6*, 737−48.
(8) Miller, D. A. B. Rationale and challenges for optical interconnects to electronic chips. *Proc. IEEE* **2000**, *88*, 728−49.
(9) Engheta, N. Circuits with light at nanoscales: optical nanocircuits inspired by metamaterials. *Science* **2007**, *317*, 1698−1702.
(10) Driscoll, T.; Kim, H. T.; Chae, B. G.; Kim, B. J.; Lee, Y. W.; Jokerst, N. M.; Palit, S.; Smith, D. R.; Di Ventra, M.; Basov, D. N. Memory metamaterials. *Science* **2009**, *325*, 1518−21.
(11) Della Giovampaola, C.; Engheta, N. Digital metamaterials. *Nat. Mater.* **2014**, *13*, 1115−21.
(12) Scalora, M.; Vincenti, M. A.; De Ceglia, D.; Roppo, V.; Centini, M.; Akozbek, N.; Bloemer, M. J. Second- and third-harmonic generation in metal-based structures. *Phys. Rev. A: At., Mol., Opt. Phys.* **2010**, *82*, 1−14.
(13) Kildishev, A. V.; Boltasseva, A.; Shalaev, V. M. Planar photonics with metasurfaces. *Science* **2013**, *339*, 1232009.
(14) Yu, N.; Capasso, F. Flat optics with designer metasurfaces. *Nat. Mater.* **2014**, *13*, 139−50.
(15) Falco, A. D.; Ploschner, M.; Krauss, T. F. Flexible metamaterials at visible wavelengths. *New J. Phys.* **2010**, *12*, 113006.
(16) Peralta, X. G.; Wanke, M. C.; Arrington, C. L.; Williams, J. D.; Brener, I.; Strikwerda, a.; Averitt, R. D.; Padilla, W. J.; Smirnova, E.; Taylor, a. J.; O'Hara, J. F. Large-area metamaterials on thin membranes for multilayer and curved applications at terahertz and higher frequencies. *Appl. Phys. Lett.* **2009**, *94*, 1−4.
(17) Feth, N.; Enkrich, C.; Wegener, M.; Linden, S. Large-area magnetic metamaterials via compact interference lithography. *Opt. Express* **2007**, *15*, 501−7.
(18) Gwinner, M. C.; Koroknay, E.; Liwei, F.; Patoka, P.; Kandulski, W.; Giersig, M.; Giessen, H. Periodic large-area metallic split-ring resonator metamaterial fabrication based on shadow nanosphere lithography. *Small* **2009**, *5*, 400−6.
(19) Aieta, F.; Genevet, P.; Yu, N.; Kats, M. A.; Gaburro, Z.; Capasso, F. Out-of-Plane Reflection and Refraction of Light by Anisotropic Optical Antenna Metasurfaces with Phase Discontinuities. *Nano Lett.* **2012**, *12*, 1702−6.
(20) Pfeiffer, C.; Emani, N. K.; Shaltout, A. M.; Boltasseva, A.; Shalaev, V. M.; Grbic, A. Efficient light bending with isotropic metamaterial Huygens' surfaces. *Nano Lett.* **2014**, *14*, 2491−7.
(21) Iyer, P. P.; Butakov, N. A.; Schuller, J. A. Reconfigurable Semiconductor Phased-Array Metasurfaces. *ACS Photonics* **2015**, *2*, 1077−84.
(22) Keren-Zur, S.; Avayu, O.; Michaeli, L.; Ellenbogen, T. Nonlinear Beam Shaping with Plasmonic Metasurfaces. *ACS Photonics* **2016**, *3*, 117−23.
(23) Karimi, E.; Schulz, S. a.; De Leon, I.; Qassim, H.; Upham, J.; Boyd, R. W. Generating optical orbital angular momentum at visible wavelengths using a plasmonic metasurface. *Light: Sci. Appl.* **2014**, *3*, e167.
(24) Wu, C.; Arju, N.; Kelp, G.; Fan, J. A.; Dominguez, J.; Gonzales, E.; Tutuc, E.; Brener, I.; Shvets, G. Spectrally selective chiral silicon metasurfaces based on infrared Fano resonances. *Nat. Commun.* **2014**, *5*, 1−9.
(25) Yin, X.; Ye, Z.; Rho, J.; Wang, Y.; Zhang, X. Photonic Spin Hall Effect at Metasurfaces. *Science* **2013**, *339*, 1405−1407.
(26) Shalaev, M. I.; Sun, J.; Tsukernik, A.; Pandey, A.; Nikolskiy, K.; Litchinitser, N. M. High-Efficiency All-Dielectric Metasurfaces for Ultracompact Beam Manipulation in Transmission Mode. *Nano Lett.* **2015**, *15*, 6261−6.
(27) Khorasaninejad, M.; Aieta, F.; Kanhaiya, P.; Kats, M. A.; Genevet, P.; Rousso, D.; Capasso, F. Achromatic Metasurface Lens at Telecommunication Wavelengths. *Nano Lett.* **2015**, *15*, 5358−62.
(28) Ni, X.; Kildishev, A. V.; Shalaev, V. M. Metasurface holograms for visible light. *Nat. Commun.* **2013**, *4*, 1−6.
(29) Sámson, Z. L.; MacDonald, K. F.; De Angelis, F.; Gholipour, B.; Knight, K.; Huang, C. C.; Di Fabrizio, E.; Hewak, D. W.; Zheludev, N. I. Metamaterial electro-optic switch of nanoscale thickness. *Appl. Phys. Lett.* **2010**, *96*, 143105.
(30) Dani, K. M.; Ku, Z.; Upadhya, P. C.; Prasankumar, R. P.; Brueck, S. R. J.; Taylor, A. J. Subpicosecond optical switching with a negative index metamaterial. *Nano Lett.* **2009**, *9*, 3565−9.
(31) Shcherbakov, M. R.; Vabishchevich, P. P.; Shorokhov, A. S.; Chong, K. E.; Choi, D.-Y.; Staude, I.; Miroshnichenko, A. E.; Neshev, D. N.; Fedyanin, A. A.; Kivshar, Y. S. Ultrafast All-Optical Switching with Magnetic Resonances in Nonlinear Dielectric Nanostructures. *Nano Lett.* **2015**, *15*, 6985−90.
(32) Minovich, A. E.; Miroshnichenko, A. E.; Bykov, A. Y.; Murzina, T. V.; Neshev, D. N.; Kivshar, Y. S. Functional and nonlinear optical metasurfaces. *Laser Photon. Rev.* **2015**, *9*, 195−213.
(33) Klein, M. W.; Enkrich, C.; Wegener, M.; Linden, S. Second-harmonic generation from magnetic metamaterials. *Science* **2006**, *313*, 502−4.
(34) Klein, M. W.; Wegener, M.; Feth, N.; Linden, S. Experiments on second- and third-harmonic generation from magnetic metamaterials. *Opt. Express* **2007**, *15*, 5238−47.
(35) Boyd, R. W. *Nonlinear Optics*, Third ed.; Academic Press: Cambridge, MA, 2008; p 78.
(36) Wang, F. X.; Rodríguez, F. J.; Albers, W. M.; Ahorinta, R.; Sipe, J. E.; Kauranen, M. Surface and bulk contributions to the second-order nonlinear optical response of a gold film. *Phys. Rev. B: Condens. Matter Mater. Phys.* **2009**, *80*, 233402.
(37) Enkrich, C.; Wegener, M.; Linden, S.; Burger, S.; Zschiedrich, L.; Schmidt, F.; Zhou, J. F.; Koschny, T.; Soukoulis, C. M. Magnetic Metamaterials at Telecommunication and Visible Frequencies. *Phys. Rev. Lett.* **2005**, *95*, 203901.
(38) Walsh, G. F.; Dal Negro, L. Enhanced second harmonic generation by photonic-plasmonic Fano-type coupling in nanoplasmonic arrays. *Nano Lett.* **2013**, *13*, 3111−7.
(39) Gay-Balmaz, P.; Martin, O. J. F. Electromagnetic resonances in individual and coupled split-ring resonators. *J. Appl. Phys.* **2002**, *92*, 2929.
(40) Baida, H.; Mongin, D.; Christofilos, D.; Bachelier, G.; Crut, A.; Maioli, P.; Del Fatti, N.; H; Vallée, F. Ultrafast nonlinear optical response of a single gold nanorod near its surface plasmon resonance. *Phys. Rev. Lett.* **2011**, *107*, 57402.
(41) Zavelani-Rossi, M.; Polli, D.; Kochtcheev, S.; Baudrion, A.-L.; Béal, J.; Kumar, V.; Molotokaite, E.; Marangoni, M.; Longhi, S.; Cerullo, G.; Adam, P.-M.; Della Valle, G. Transient optical response of a single gold nanoantenna: the role of plasmon detuning. *ACS Photonics* **2015**, *2*, 521−529.
(42) Ginzburg, P.; Krasavin, A.; Sonnefraud, Y.; Murphy, A.; Pollard, R. J.; Maier, S. A.; Zayats, A. V. Nonlinearly coupled localized plasmon resonances: Resonant second-harmonic generation. *Phys. Rev. B: Condens. Matter Mater. Phys.* **2012**, *86*, 85422.
(43) Celebrano, M.; Wu, X.; Baselli, M.; Großmann, S.; Biagioni, P.; Locatelli, A.; De Angelis, C.; Cerullo, G.; Osellame, R.; Hecht, B.; Duò, L.; Ciccacci, F.; Finazzi, M. Mode matching in multiresonant plasmonic nanoantennas for enhanced second harmonic generation. *Nat. Nanotechnol.* **2015**, *10*, 412−417.

DOI: 10.1021/acsphotonics.6b00108
ACS Photonics 2016, 3, 1517−1522